

# Scaling of Tip Vortex Cavitation Inception Noise With a Bubble Dynamics Model Accounting for Nuclei Size Distribution

Chao-Tsung Hsiao

e-mail: ctsung@dynaflo-inc.com

Georges L. Chahine

e-mail: glchahine@dynaflo-inc.com

Dynaflo, Inc.

10621-J Iron Bridge Road, Jessup, MD 20794

*The acoustic pressure generated by cavitation inception in a tip vortex flow was simulated in water containing a realistic bubble nuclei size distribution using a surface-averaged pressure (SAP) spherical bubble dynamics model. The flow field was obtained by the Reynolds-averaged Navier–Stokes computations for three geometrically similar scales of a finite-span elliptic hydrofoil. An “acoustic” criterion, which defines cavitation inception as the flow condition at which the number of acoustical “peaks” above a pre-selected pressure level exceeds a reference number per unit time, was applied to the three scales. It was found that the scaling of cavitation inception depended on the reference values (pressure amplitude and number of peaks) selected. Scaling effects (i.e., deviation from the classical  $\sigma_i \propto R_e^{0.4}$ ) increase as the reference inception criteria become more stringent (lower threshold pressures and less number of peaks). Larger scales tend to detect more cavitation inception events per unit time than obtained by classical scaling because a relatively larger number of nuclei are excited by the tip vortex at the larger scale due to simultaneous increase of the nuclei capture area and of the size of the vortex core. The average nuclei size in the nuclei distribution was also found to have an important impact on cavitation inception number. Scaling effects (i.e., deviation from classical expressions) become more important as the average nuclei size decreases. [DOI: 10.1115/1.1852476]*

## 1 Introduction

Scaling of the results of a propeller tip vortex cavitation inception studies from laboratory to large scales has not always been very successful. Aside from the problems associated with properly scaling the flow field, existing scaling laws as derived or used by previous studies, e.g., [1–6], lack the ingredients necessary to explain sometimes major discrepancies between model and full scale. One of the major aspects which has not been appropriately incorporated in the scaling law is nuclei presence and nuclei size distribution effects. Another issue which may cause scaling problems is the means of detection of cavitation inception. Practically, the flow condition is considered to be at cavitation inception when either an “acoustic” criterion or an “optical” criterion is met [7,8]. These two detection methods are known to provide different answers in the most practical applications. Furthermore, for practical reasons inception may be detected by one method at model scale and by another at full scale. To address this issue in a more consistent manner for different scales, the present study considers an “acoustic” criterion which determines the cavitation inception event by counting the number of acoustical signal peaks that exceed a certain level in unit time.

To theoretically address the above issues in a practical way spherical bubble dynamics models were adopted in many studies in order to simulate the bubble dynamics and to predict tip vortex cavitation inception [8–10]. In our previous studies [8,11], an improved surface-averaged pressure (SAP) spherical bubble dynamics model was developed and applied to predict single bubble trajectory, size variation and resulting acoustic signals. This model was later shown to be much superior than the classical spherical model through its comparison to a two-way fully three-dimensional (3D) numerical model which includes bubble shape

deformation and the full interaction between the bubble and the viscous flow field [11]. In the present study we incorporate the SAP spherical bubble dynamics model with a statistical nuclei distribution in order to enable prediction of cavitation inception in a practical liquid flow field with known nuclei size distribution. This is realized by randomly distributing the nuclei in space and time according to the given nuclei size distribution. According to previous studies [12,13] the number of nuclei to use in the computation can be reduced by considering only the nuclei that pass through a so-called “window of opportunity” and are captured by the tip vortex.

In order to study scale effects in a simple vortex flow field we consider the tip vortex flows generated by a set of three geometrically similar elliptic hydrofoils. The flow fields are obtained by steady-state Navier–Stokes computations which provide the velocity and pressure fields for the bubble dynamics computations. The SAP spherical model is then used to track all nuclei released randomly in time and space from the nuclei release area and to record the acoustic signals generated by their dynamics and volume oscillations.

## 2 Numerical Models

**2.1 Navier–Stokes Computations.** To best describe the tip vortex flow field around a finite-span hydrofoil, the Reynolds-averaged Navier–Stokes (RANS) equations with a turbulence model are solved. These have been shown to be successful in addressing tip vortex flows [14] and general propulsor flows [15,16]. The three-dimensional unsteady Reynolds-averaged incompressible continuity and Navier–Stokes equations in nondimensional form and Cartesian tensor notations are written as

$$\frac{\partial u_i}{\partial x_i} = 0 \quad (1)$$

Contributed by the Fluids Engineering Division for publication on the JOURNAL OF FLUIDS ENGINEERING. Manuscript received by the Fluids Engineering Division September 13, 2003; revised manuscript received August 13, 2004. Review Conducted by: S. Ceccio.

$$\frac{\partial u_i}{\partial t} + u_j \frac{\partial u_i}{\partial x_j} = -\frac{\partial p}{\partial x_i} + \frac{\partial \tau_{ij}}{\partial x_j} \quad (2)$$

where  $u_i = (u, v, w)$  are the Cartesian components of the velocity,  $x_i = (x, y, z)$  are the Cartesian coordinates,  $p$  is the pressure,  $Re = \rho u^* L^* / \mu$  is the Reynolds number,  $u^*$  and  $L^*$  are the characteristic velocity and length selected to be, respectively, the free stream velocity,  $V_\infty$  and root chord length,  $C_0$ .  $\rho$  is the liquid density, and  $\mu$  is its dynamic viscosity. The effective stress tensor  $\tau_{ij}$  is given by

$$\tau_{ij} = \frac{1}{Re} \left[ \left( \frac{\partial u_i}{\partial x_j} + \frac{\partial u_j}{\partial x_i} \right) - \frac{2}{3} \delta_{ij} \frac{\partial u_k}{\partial x_k} \right] - \overline{u_i u_j} \quad (3)$$

where  $\delta_{ij}$  is the Kronecker delta and  $\overline{u_i u_j}$  is the Reynolds stress tensor resulting from the Reynolds averaging scheme.

To numerically simulate the tip vortex flow around a finite-span hydrofoil, a body-fitted curvilinear grid is generated and Eqs. (1) and (2) are transformed into a general curvilinear coordinate system. The transformation provides a computational domain that is better suited for applying the spatial differencing scheme and the boundary conditions. To solve the transformed equations, we use the three-dimensional incompressible Navier–Stokes flow solver, DF\_UNCLE, derived from the code UNCLE developed at Mississippi State University. The DF\_UNCLE code is based on the artificial-compressibility method [17] which a time derivative of the pressure multiplied by an artificial-compressibility factor is added to the continuity equation. As a consequence, a hyperbolic system of equations is formed and is solved using a time marching scheme in pseudo-time to reach a steady-state solution.

The numerical scheme in DF\_UNCLE uses a finite volume formulation. First-order Euler implicit differencing is applied to the time derivatives. The spatial differencing of the convective terms uses the flux-difference splitting scheme based on Roe's method [18] and van Leer's MUSCL method [19] for obtaining the first-order and the third-order fluxes, respectively. A second-order central differencing is used for the viscous terms which are simplified using the thin-layer approximation. The flux Jacobians required in the implicit scheme are obtained numerically. The resulting system of algebraic equations is solved using the Discretized Newton Relaxation method [20] in which symmetric block Gauss–Seidel sub-iterations are performed before the solution is updated at each Newton interaction. A  $k-\varepsilon$  turbulence model is used to model the Reynolds stresses in Eq. (3).

All boundary conditions in DF\_UNCLE are imposed implicitly. Here, a free stream constant velocity and pressure condition is specified at all far-field side boundaries. The method of characteristic is applied at the inflow boundary with all three components of velocities specified while a first-order extrapolation for all variables is used at the outflow boundary. On the solid hydrofoil surface, a no-slip condition and a zero normal pressure gradient condition are used. At the hydrofoil root boundary, a plane symmetry condition is specified.

**2.2 Statistical Nuclei Distribution Model.** In order to address a realistic liquid condition in which a liquid flow field contains a distribution of nuclei with different sizes, a statistical nuclei distribution is used. We consider a liquid with a known nuclei size density distribution function,  $n(R)$ .  $n(R)$  is defined as the number of nuclei per cubic meter having radii in the range  $[R, R + \delta R]$ . This function has a unit  $m^{-4}$  and is given by

$$n(R) = \frac{dN(R)}{dR} \quad (4)$$

where  $N(R)$  is the number of nuclei of radius  $R$  in a unit volume. This function can be obtained from experimental measurements such as light scattering, cavitation susceptibility meter and ABS Acoustic Bubble Spectrometer® measurements [21] and can be expressed as a discrete distribution of  $M$  selected nuclei sizes. Thus, the total void fraction,  $\alpha$ , in the liquid can be obtained by

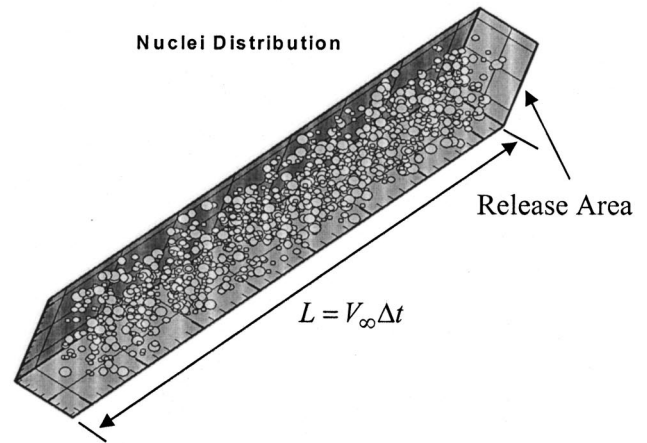
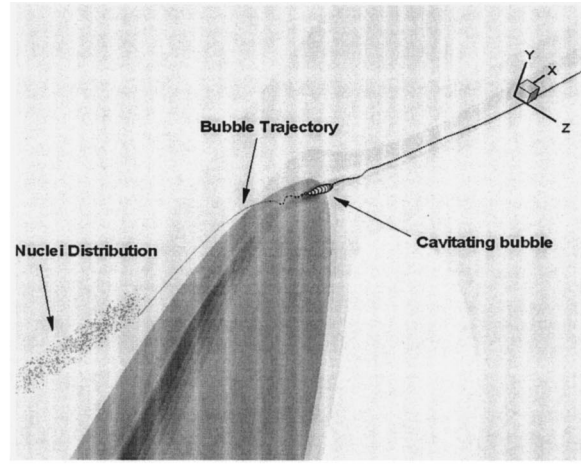


**Fig. 1 The location and size of a fictitious volume for randomly distributing the nuclei**

$$\alpha = \sum_{i=1}^M N_i \frac{4\pi R_i^3}{3} \quad (5)$$

where  $N_i$  is the discrete number of nuclei of radius  $R_i$  used in the computations. The position and timing of nuclei released in the flow field are obtained using random distribution functions, always ensuring that the local and overall void fraction satisfy the nuclei size distribution function.

From previous studies [12,13], we know that only nuclei that “enter” a given region or “window of opportunity” are actually captured by the vortex and generate strong acoustic signals. Therefore, it is economical to consider only nuclei emitted from this “window of opportunity.” This is similar to considering a fictitious volume of cross area equal to the window area and of length equal to  $V_\infty \Delta t$ , where  $V_\infty$  is the free stream velocity and  $\Delta t$  is the total time of signal acquisition (see Fig. 1).

**2.3 Bubble Dynamics.** The nuclei convected in the flow field are treated using a spherical bubble dynamics model. To do so, we use the Rayleigh–Plesset equation modified to account for a slip velocity between the bubble and the host liquid, and for the nonuniform pressure field along the bubble surface [10]. The resulting modified surface-averaged pressure (SAP) Rayleigh–Plesset equation can be written as:

$$R\ddot{R} + \frac{3}{2}\dot{R}^2 = \frac{1}{\rho} \left( p_v + p_{g0} \left( \frac{R_0}{R} \right)^{3k} - P_{\text{encounter}} - \frac{2\gamma}{R} - \frac{4\mu\dot{R}}{R} \right) + \frac{(\mathbf{u} - \mathbf{u}_b)^2}{4} \quad (6)$$

where  $R$  is the time varying bubble radius,  $R_0$  is the initial or reference bubble radius,  $\gamma$  is the surface tension parameter,  $p_v$  is the vapor pressure,  $p_{g0}$  is the initial or reference gas pressure inside the bubble, and  $k$  is the polytropic compression law constant.  $\mathbf{u}$  is the liquid convection velocity and  $\mathbf{u}_b$  is the bubble travel velocity.  $P_{\text{encounter}}$  is the ambient pressure “seen” by the bubble during its travel. In the SAP method  $P_{\text{encounter}}$  is defined as the average of the liquid pressures over the bubble surface [11].

The bubble trajectory is obtained using the following motion equation [22]

$$\frac{d\mathbf{u}_b}{dt} = \frac{3}{\rho} \nabla P + \frac{3}{4} C_D (\mathbf{u} - \mathbf{u}_b) |\mathbf{u} - \mathbf{u}_b| + \frac{3}{R} (\mathbf{u} - \mathbf{u}_b) \dot{R} \quad (7)$$

where the drag coefficient  $C_D$  is given by an empirical equation such as that of Haberman and Morton [23]

$$C_D = \frac{24}{R_{eb}} (1 + 0.197R_{eb}^{0.63} + 2.6 \times 10^{-4} R_{eb}^{1.38}); \quad R_{eb} = \frac{2\rho R |\mathbf{u} - \mathbf{u}_b|}{\mu} \quad (8)$$

The pressure at a distance  $l$  from the bubble center generated by the bubble dynamics is given by the expression

$$p = \frac{\rho}{l} [R^2 \ddot{R} + 2R \dot{R}^2] - \rho \left[ \frac{R^4 \dot{R}^2}{2l^4} \right] \quad (9)$$

When  $l \gg R$ , Eq. (9) becomes the expression for the acoustic pressure  $p_a$  of Fitzpatrick and Strasberg [24] after introduction of the delayed time  $t'$  due to a finite sound speed,  $c$

$$p_a(t') = \frac{R\rho}{l} [R\ddot{R}(t') + 2\dot{R}^2(t')], \quad t' = t - \frac{r-R}{c} \quad (10)$$

To determine the bubble motion and its volume variation, a Runge–Kutta fourth-order scheme is used to integrate Eqs. (6) and (7) through time. The liquid velocity and pressures are obtained directly from the RANS computations. The numerical solution of the RANS equations, however, offers the solution directly only at the grid points. To obtain the values for any specified location  $(x, y, z)$  on the bubble we need to interpolate from the background grid. To do so, an interpolation stencil and interpolation coefficients at any specified location are determined at each time step. We use a three-dimensional point-locating scheme based on the fact that the coordinates  $(x, y, z)$  of the bubble location are uniquely represented relative to the eight corner points of the background grid stencil by

$$x = \sum_{i=1}^8 N_i \bar{x}_i, \quad y = \sum_{i=1}^8 N_i \bar{y}_i, \quad z = \sum_{i=1}^8 N_i \bar{z}_i, \quad (11)$$

where

$$\begin{aligned} N_1 &= (1-\phi)(1-\psi)(1-\varphi), & N_2 &= \phi(1-\psi)(1-\varphi), \\ N_3 &= (1-\phi)\psi(1-\varphi), & N_4 &= \phi\psi(1-\varphi), \\ N_5 &= (1-\phi)(1-\psi)\varphi, & N_6 &= \phi(1-\psi)\varphi, \\ N_7 &= (1-\phi)\psi\varphi, & N_8 &= \phi\psi\varphi. \end{aligned} \quad (12)$$

$\phi, \psi, \varphi$  are the interpolation coefficients, and  $(\bar{x}_i, \bar{y}_i, \bar{z}_i)$  are the coordinates of the eight corner points of a grid stencil in the background grid. Equation (11) is solved using a Newton–Raphson method. For a bubble point to be inside the grid stencil requires that the corresponding  $\phi, \psi, \varphi$  satisfy  $0 \leq \phi \leq 1, 0 \leq \psi \leq 1, 0 \leq \varphi \leq 1$ .

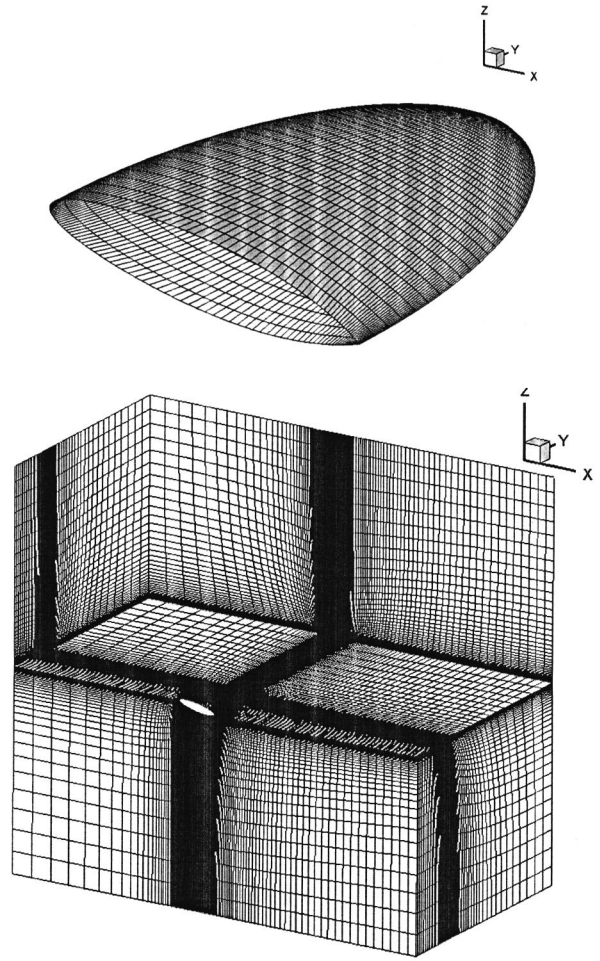


Fig. 2 Computational domain and grid for the current study

Once the interpolation stencil and interpolation coefficients are determined, the pressure and velocities can be obtained by using a similar equation to Eq. (11).

**2.4 Computational Domain and Grid Generation.** To compute the flow around the finite-span elliptic hydrofoil we generated an H–H type grid with a total of 2.7 million grid points in which  $191 \times 101 \times 101$  grid points were created in the streamwise, spanwise and normal direction, respectively, and  $81 \times 61$  grid points were used to discretize the hydrofoil surface. The grid is subdivided into 12 blocks for a computational domain which has all far-field boundaries located six (6) chord lengths away from the hydrofoil surface (see Fig. 2). Grid resolution was determined according to previous numerical studies [14,25] in which extensive investigations of the grid resolution for the tip vortex flow showed that the minimum number of grid points needed for good resolution is at least 15 grid points across the vortex core. Here, the grid resolution for the tip vortex was optimized through repeated computations and regridding to align grid clustering around the tip vortex centerline. The final refined grid selected for the results shown below had at least 16 grid points in the spanwise direction and 19 grid points in the crosswise direction within the vortex core. The first grid above the hydrofoil surface was located such that  $y^+ \approx 1$  in order to properly apply the turbulence model.

### 3 Results

**3.1 3D Steady-State Tip Vortex Flow.** The selected finite-span elliptic foil has a NACA16020 cross section with an aspect ratio of 3 (based on semispan). The flow field at an angle of attack

**Table 1 Characteristics of the three NACA16020 foil used**

	Small scale	Medium scale	Large scale
$C_0$	0.144 m	0.288 m	0.576 m
$V_\infty$	10 m/s	10 m/s	10 m/s
$Re$	$1.44 \times 10^6$	$2.88 \times 10^6$	$5.76 \times 10^6$
$-C_{p_{min}}$	3.34	4.34	5.48

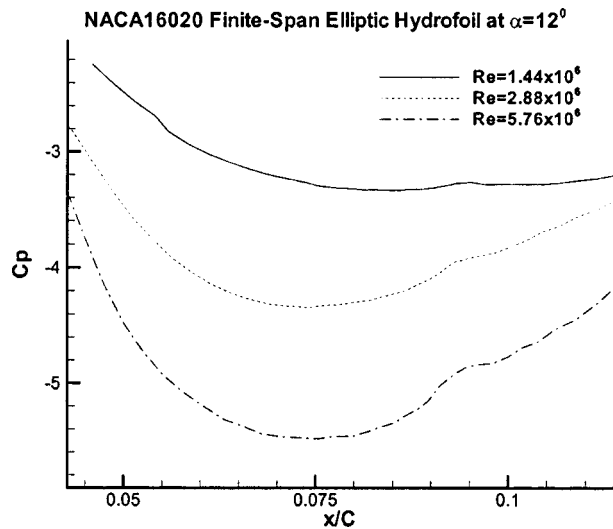


**Fig. 3 Pressure coefficient variations along the NACA16020 elliptic foil for three values of the Reynolds number**

of 12 deg was computed for three foil sizes or three different Reynolds numbers in order to study cavitation scaling effects. These correspond to the three scales shown in Table 1. In all three cases a steady-state solution was considered achieved when  $\nabla \cdot \bar{V} \leq 1 \times 10^{-4}$ . The resulting pressure coefficients along the tip vortex centerline are shown in Fig. 3. It is seen that the locations of the minimum pressure for all three cases are very close to the hydrofoil tip and are located at  $x/C_0 = 0.085, 0.075,$  and  $0.075$ . The corresponding minimum pressure coefficients are shown in Table 1. If the cavitation inception number is assumed to be  $-C_{p_{min}}$ , then these values correlate with the power formulation:  $\sigma_i \propto Re^{0.36}$ .

To validate the steady state computations an additional case was computed at an angle of attack equal to  $10^\circ$  and  $Re = 4.75 \times 10^6$ . The results were compared to the available experimental measurements of [2] by considering the tangential and axial velocity components across the tip vortex core at two streamwise locations. As seen in Fig. 4, the comparison indicates that the tip vortex flow is well predicted in the near-field region in which the pressure coefficient along the vortex center reaches its minimum. However, over-diffusion in vortex core size and over-dissipation in velocities are seen for the numerical solution further downstream especially for the axial velocity component whose velocity profile changes from excess to deficit. Notice, however, that this occurs beyond the region of interest here for bubble dynamics studies. Indeed, the bubble dynamics simulations show that the bubble growth and collapse durations are relatively very short (see Fig. 5) and occur before  $x/C_0 = 0.1$ . In this region, our numerical solution

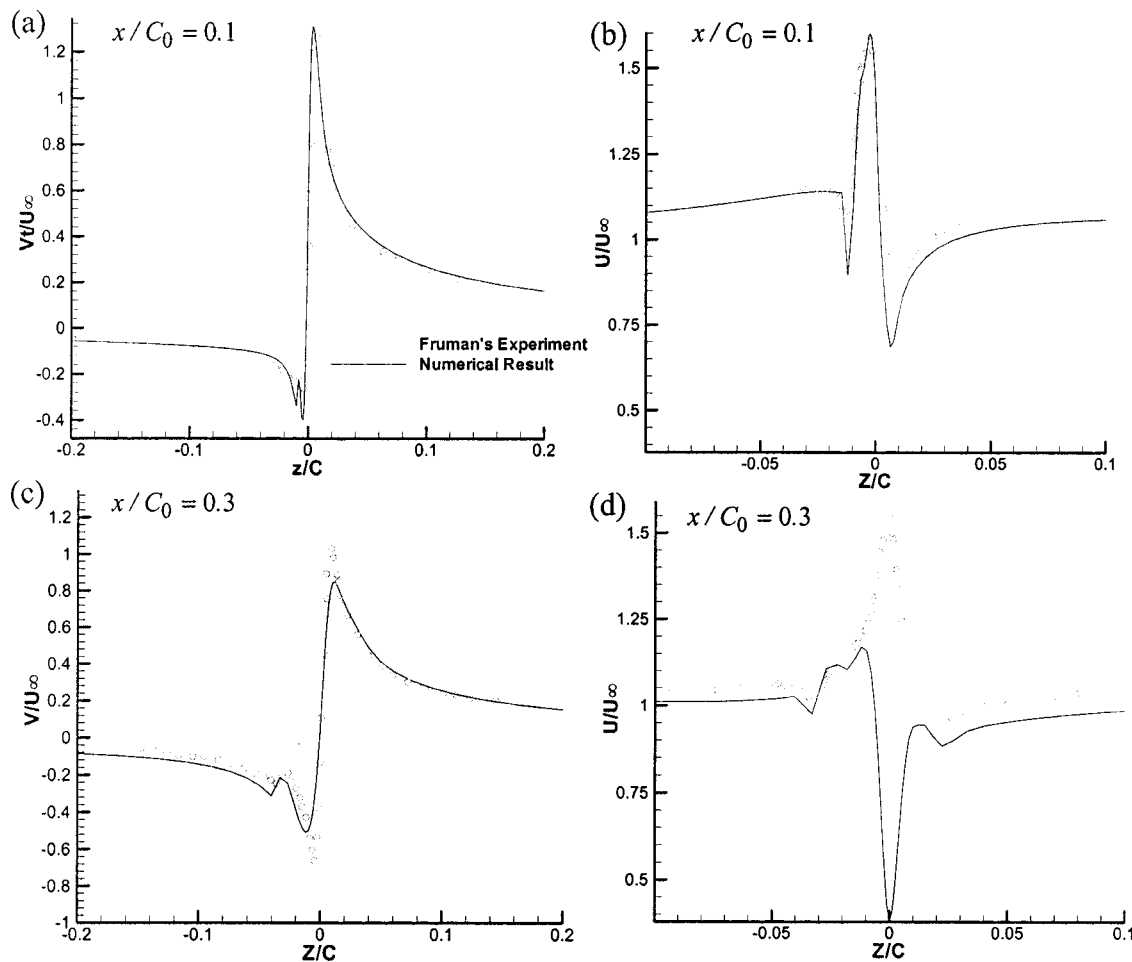


**Fig. 4 Comparison of tangential and axial velocity components across the tip vortex core at  $x/C_0 = 0.1$  and  $0.3$  between present numerical result and experimental measurements (Fruman et al. 1992)**

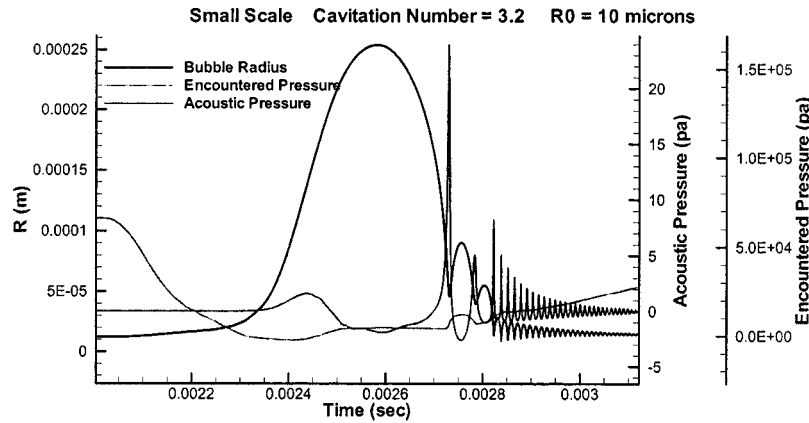


Fig. 5 Example computation of bubble dynamics for bubble radius, encountered pressure, and emitted acoustic pressure versus time during bubble capture in the tip vortex

agrees quite well with the experimental measurements. Therefore, the present Navier–Stokes computations are reliable for studying the bubble behavior in the  $Cp_{\min}$  region of interest.

**3.2 Window of Opportunity.** The “window of opportunity” can be determined by releasing nuclei upstream of the foils and tracking their trajectories to see if they enter into the low pressure areas in the tip vortex flow. A release plane located at  $x/C_0 = -0.1$  ahead of the hydrofoil tip ( $x/C_0 = 0$ ) was used. Nuclei were released from this plane at various locations, tracked, and the minimum pressure they encountered is recorded at the corresponding release point.

Initially, 300 nuclei of a given size were released from the release plane. All properties are defined at 20°C. The cavitation number was specified high enough such that the maximum growth size of nucleus was less than 10%. Figure 6 shows a contour plot of the minimum pressure coefficient encountered for each release location for different nuclei sizes in the small scale. The contours are blanked out for the release points where the nuclei collide with the hydrofoil surface. It is seen that the size of the “window of opportunity” becomes smaller and its location shifts closer to the hydrofoil surface of pressure side when the nuclei sizes decrease. The contours of minimum encounter pressure coefficient for dif-

ferent scales with the same initial nuclei size are shown in Fig. 7. It is seen that the size of the “window of opportunity” increases as the scale increases. This implies that larger scales capture more nuclei into the vortex for the same nuclei sizes and duration of observation time when compared to smaller scales.

**3.3 Statistical Nuclei Size Distribution.** Nuclei size distribution studies in water tunnels, lakes and oceans [26,27] show a power-law distribution for the number density distribution function, with  $n(R) \approx 1/R^\beta$ , where the exponent  $\beta$  lies between 2.5 and 4. In the present study we consider a nuclei size distribution ranging from 10 to 100  $\mu\text{m}$  with a void fraction  $\alpha \approx 1 \times 10^{-6}$  as shown in Fig. 8. In order to consider a same bubble population for all scales, we have accounted for the fact that a bubble will change its radius in a static equilibrium fashion when the ambient pressure is changed. Therefore, for the same scaled cavitation number, initial nuclei sizes are reduced for the larger scales where the ambient pressure would be larger. This is not a major change in the values since gas pressure inside the bubble varies like the cube of the radius, while surface tension which is predominant varies like the inverse of the radius. This results in nuclei sizes

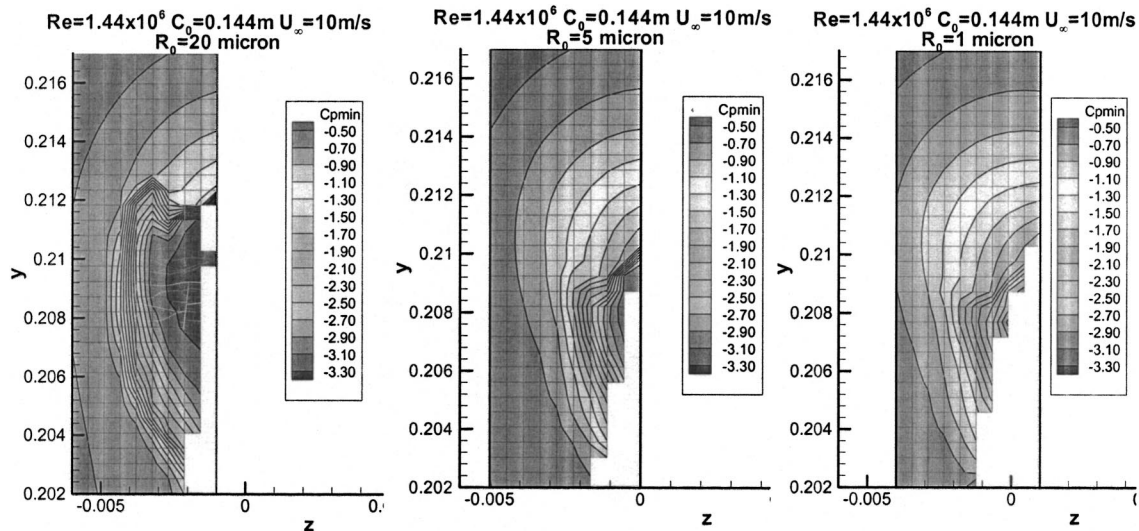


Fig. 6 Contours of the minimum pressure coefficient encountered at high cavitation number for different nuclei size in the small foil scale

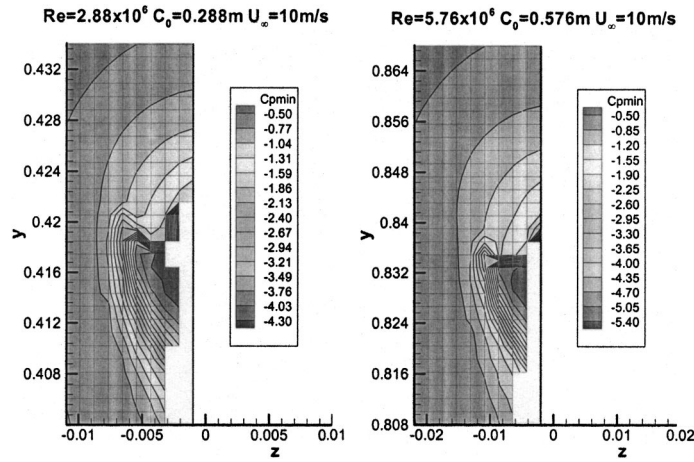


Fig. 7 Contours of the minimum pressure coefficient encountered at high cavitation number for  $R_0=20 \mu\text{m}$  and for the medium and large foil scale

ranging from 10 to 100  $\mu\text{m}$  for the small scale, 9.2–92  $\mu\text{m}$  for the medium scale, and from 8.5 to 85  $\mu\text{m}$  for the large scale. These curves are used to generate the nuclei field.

With the void fraction and size distribution provided, the total number of nuclei released for each scale is then determined based on the length of signal acquisition time and the size of the release area. To determine an appropriate statistically meaningful observation time we tested two different signal acquisition times  $\Delta t = 0.2$  and 1 s. Both cases were conducted for the small scale at cavitation number  $\sigma=3.0$ . The number of nuclei released and the number of nuclei reaching critical (cavitating) condition versus nuclei size for these two cases are shown in Fig. 9. In this figure a nucleus is considered to be a cavitation bubble when  $P_{\text{encounter}} < P_{\text{cr}}$ , where the critical pressure is defined as

$$P_{\text{cr}} = p_v - (3k-1) \left( \frac{2\gamma}{3k} \right)^{3k/3k-1} (p_{g0} R_0^{3k})^{-1/3k-1} \quad (13)$$

with  $k=1.4$ . Comparison between these two cases shows that the smaller acquisition time only results in a slightly smaller probability for cavitation. Therefore,  $\Delta t=0.2$  second is statistically sufficient and was used for the other tests. For the release window, we consider an area to be large enough to cover the “windows of opportunity” for all nuclei sizes released. Here, the size of the release area is specified as 7 mm $\times$ 5 mm, 14 mm $\times$ 10 mm, and 28

mm $\times$ 20 mm for the small, medium, and large scale, respectively. As a result, the number of nuclei in each population is 142, 568, and 2272 for the three scales, respectively.

**3.4 Scaling of Cavitation Inception Noise.** As nuclei travel in the computational domain, the resulting acoustic pressure is monitored. The acoustic pressure was computed at a location 0.3 m away from the hydrofoil tip for all cases. A series of computa-

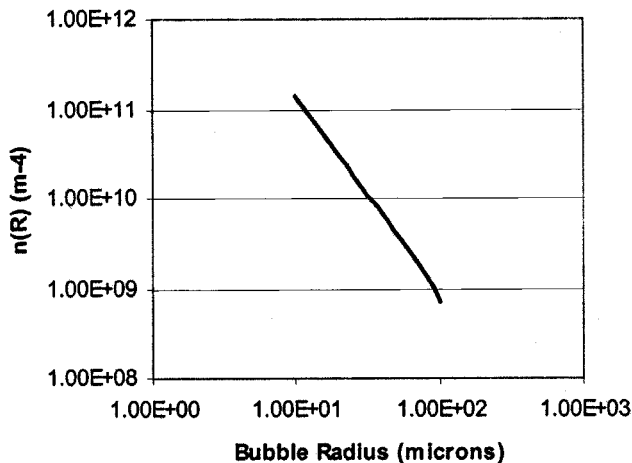


Fig. 8 Nuclei size number density distributions applied at the three scales

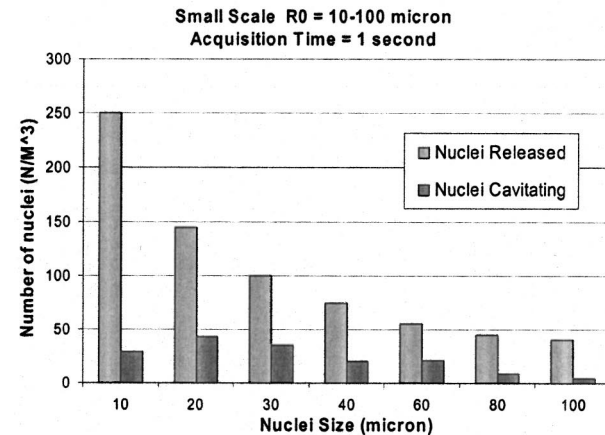
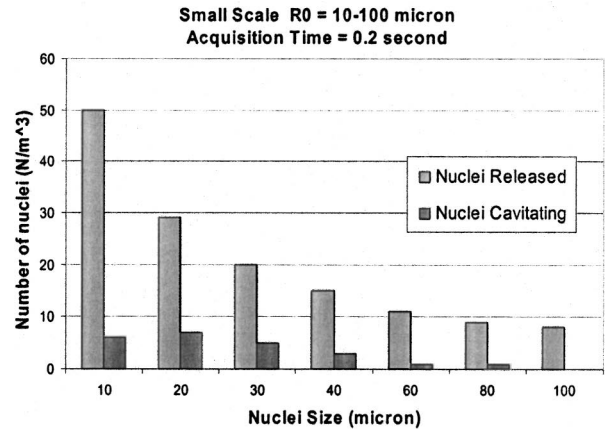


Fig. 9 The number of nuclei released and the number of nuclei reaching critical pressure (cavitating) versus nuclei size obtained at  $\sigma=3.0$  for two different acquisition times

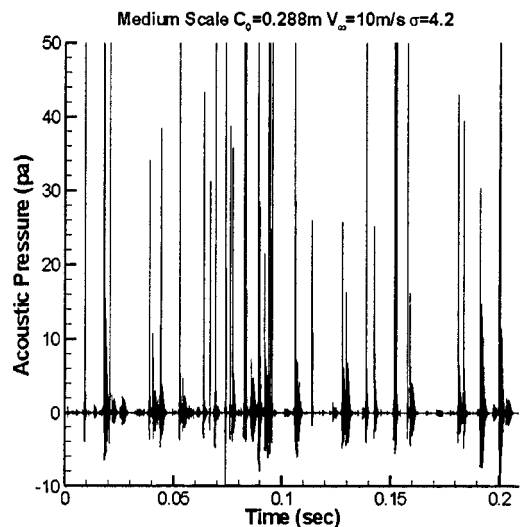
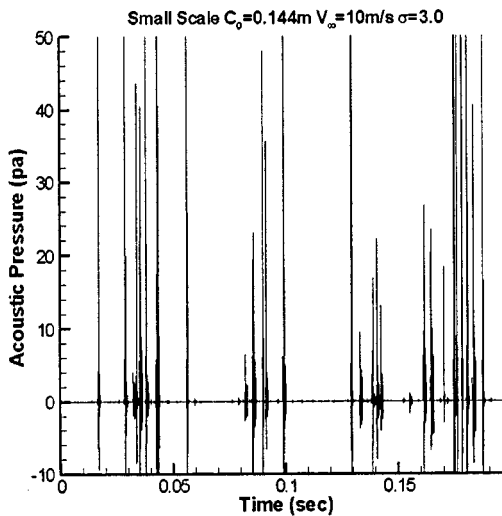
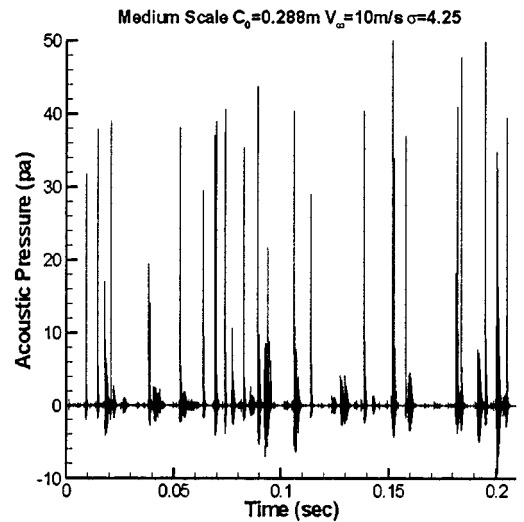
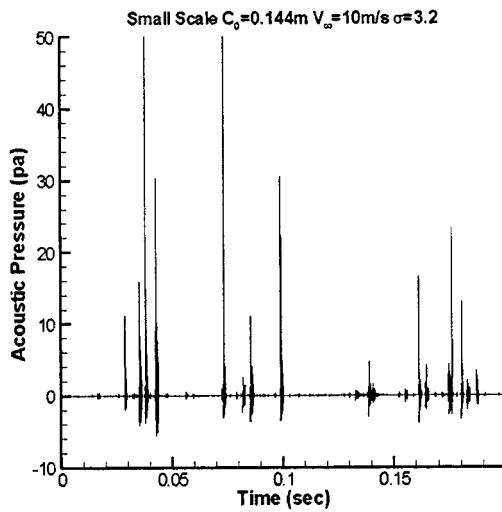
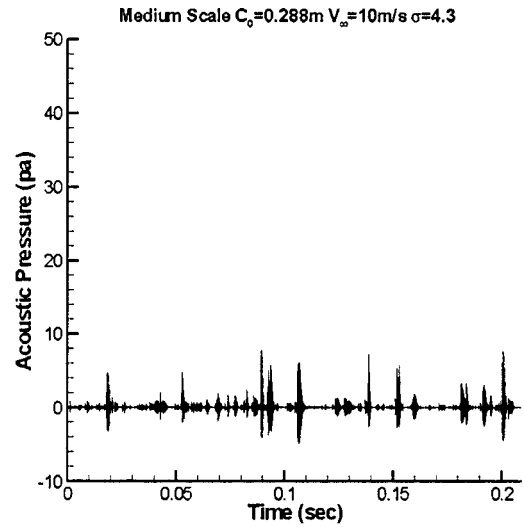
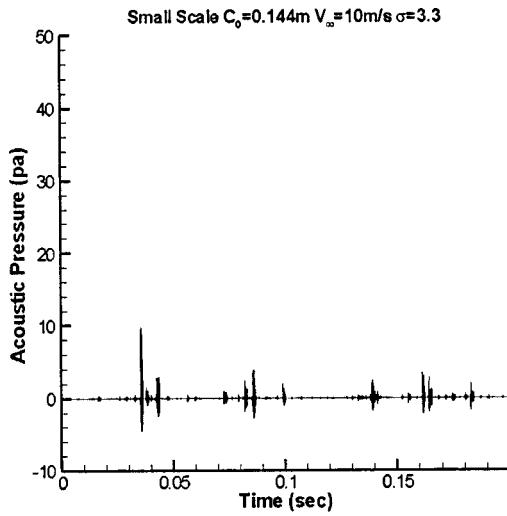


Fig. 10 The acoustic signals for the small scale at three different cavitation numbers

Fig. 11 The acoustic signals for the medium scale at three different cavitation numbers

tions were conducted at different cavitation numbers for the three scales to obtain the acoustic signals for conditions above and below cavitation inception. Figures 10–12 illustrate the acoustic signals for three different scales at three different cavitation numbers. High-level peaks of acoustic signals are clearly seen when the

cavitation number is near the cavitation inception number. It is seen that, as expected, for all scales the number of high-level peaks increases as the cavitation number decreases. However, the larger scale is more sensitive to cavitation number changes since

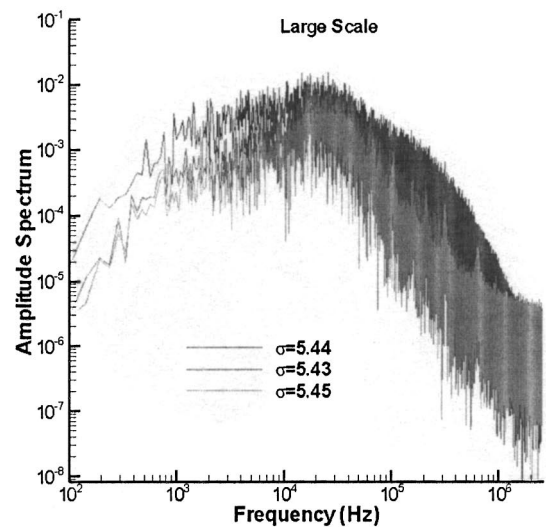
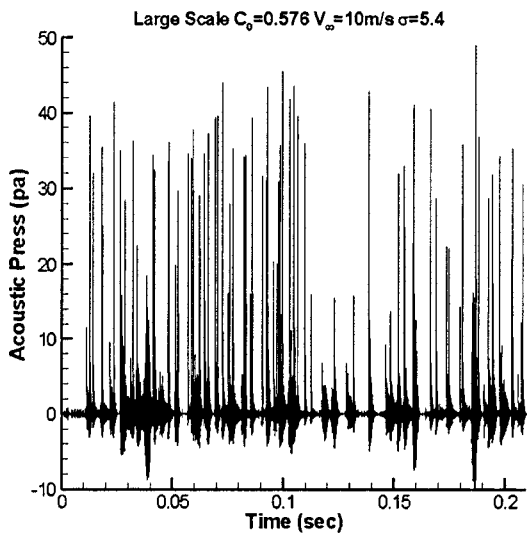
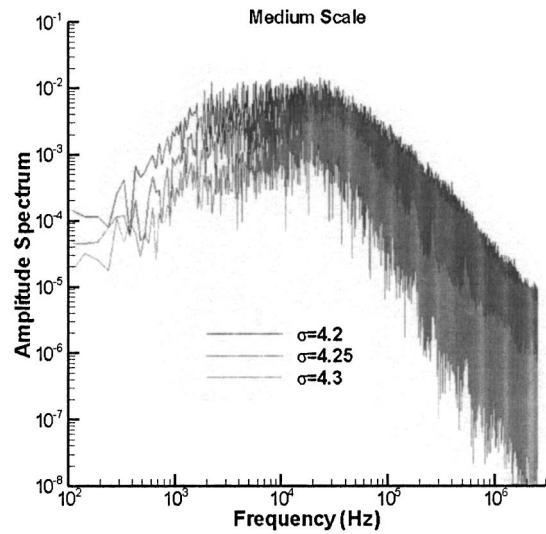
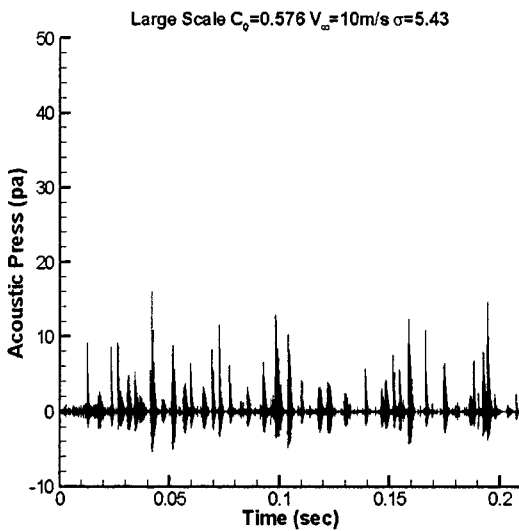
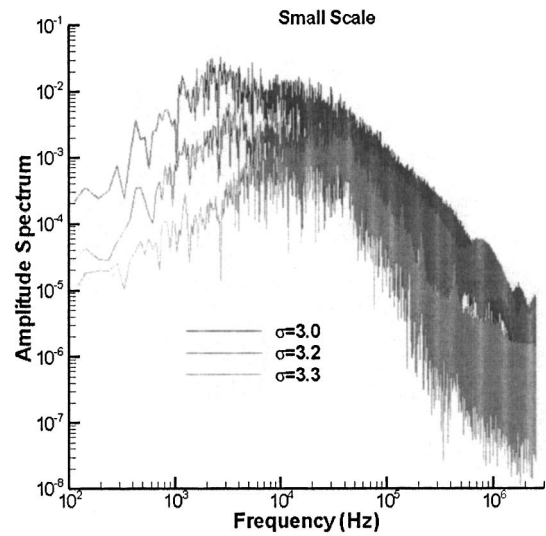
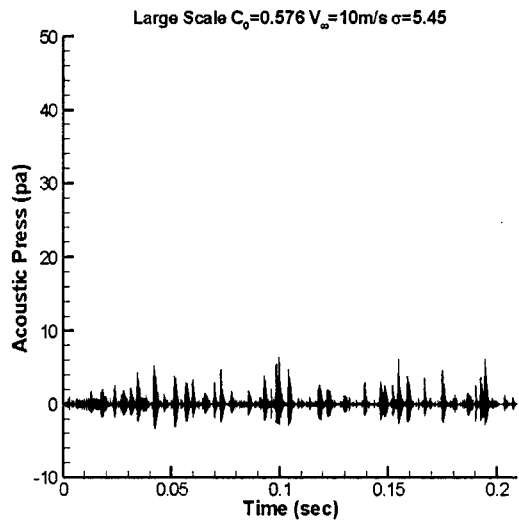


Fig. 12 The acoustic signals for the large scale at three different cavitation numbers

Fig. 13 Amplitude spectra for all three scales at three different cavitation numbers

the number of peaks increases much faster than for the smaller scale as the cavitation number decreases. Figure 13 shows the resulting frequency spectra for the acoustic signals shown in Figs.

10–12. A peak in the frequency range 30–40 kHz is seen at all scales. The amplitude of this peak increases as the cavitation number decreases.

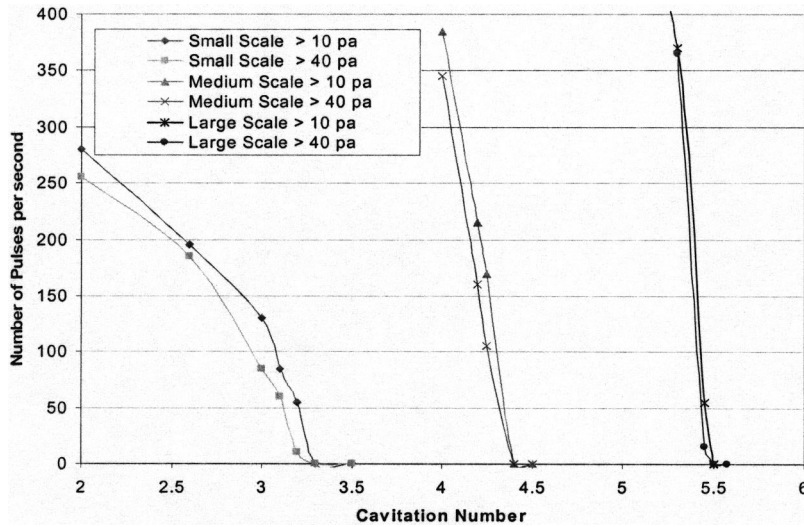


Fig. 14 Number of pressure peaks versus cavitation number deduced at two criteria of acoustic level for the three scales considered

Based on the results shown in Figs. 10–12, we can define a cavitation inception number based on the number of acoustical signal peaks per unit time that exceed a certain level. To deduce the cavitation inception number based on this criterion, a curve for the number of pressure peaks higher than a give acoustic pressure level is created for each cavitation number and for the three scales. Figure 14 shows such curves with two acoustic pressure levels, 10 and 40 Pa, are chosen for each scale. Given a selected criterion based on the number of peaks and acoustic pressure level, one can determine the cavitation inception number from Fig. 14.

The deduced cavitation inception numbers of the three scales for the criteria: 10 peaks/s over 10 Pa and 50 peaks/s over 40 Pa, are shown in Table 2. The deduced cavitation numbers and  $-Cp_{\min}$  are fitted with the classical power formula  $\sigma_i \propto R_e^\gamma$ , and the fitted values of  $\gamma$  are also shown in Table 2. It is seen that different criteria for defining the cavitation inception event can lead to different cavitation inception numbers and different scaling laws. The scaling effect due to the nuclei can be demonstrated by comparing the deduced inception number with  $-Cp_{\min}$ . The results in Table 2 show that cavitation inception scaling deviates more from  $-Cp_{\min}$  when the reference inception criterion becomes less stringent (higher reference pressure amplitude and larger number of peaks). Furthermore, the predicted value of  $\gamma$  is closer to the classical value ( $\gamma=0.4$ ), as the reference inception criterion becomes less stringent. This agrees with many experi-

Table 2 Cavitation inception numbers obtained from the numerical study using various criteria, and power law fit deduced from these results

	Numerical computed values for $\sigma_i$			$R_e^\gamma$ curve fit	
	Small scale	Medium scale	Large scale	$\gamma$	Square of correlation coefficient
$-Cp_{\min}$	3.34	4.34	5.48	0.357	0.999
10 peaks/s over 10 Pa	3.28	4.33	5.47	0.369	0.998
50 peaks/s over 40 Pa	3.12	4.28	5.44	0.401	0.994

mental studies usually established in laboratory conditions where background noise and detection techniques lead to high values of the pressure amplitude for inception detection.

**3.5 Nuclei Size Distribution Effect.** To illustrate how different nuclei size distributions influence the prediction of cavitation inception, a much finer nuclei size distribution ranging from 1 to 10  $\mu\text{m}$  is tested. In the computations the total number of nuclei released in each case was kept the same. This results in a much smaller void fraction ( $\alpha \approx 1 \times 10^{-9}$ ) than in the previous case. Figure 15 shows the acoustical signal obtained at  $\sigma=3.0$  and the number of nuclei cavitating for each prescribed nuclei size is shown in Fig. 16. It is seen that, as expected, the number of peaks is dramatically reduced for the smaller nuclei size range when comparing the results to those of the larger nuclei size range. That is because as shown in Fig. 16 near inception the nuclei contributing to the high-level peaks are only the larger bubble sizes.

A series of computations were also conducted at different cavitation numbers for the small and the large scale with the smaller

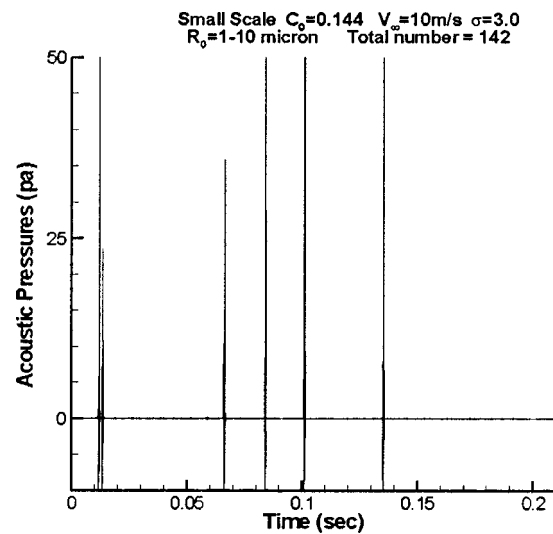


Fig. 15 The acoustic signals for the small scale at  $\sigma=3.0$  using the smaller nuclei size range (1–10  $\mu\text{m}$ )

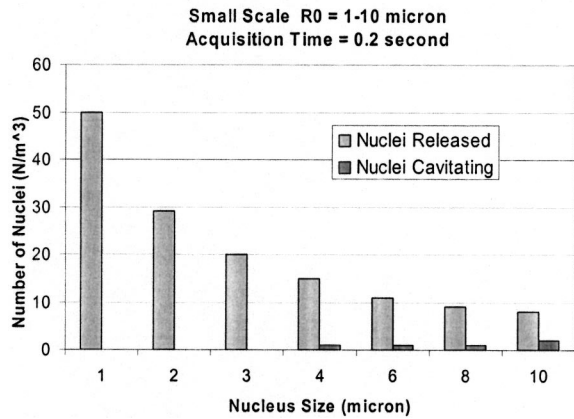


Fig. 16 The number of nuclei released and the number of nuclei cavitating versus nuclei size obtained for the 1–10  $\mu\text{m}$  small nuclei size distribution at  $\sigma=3.0$

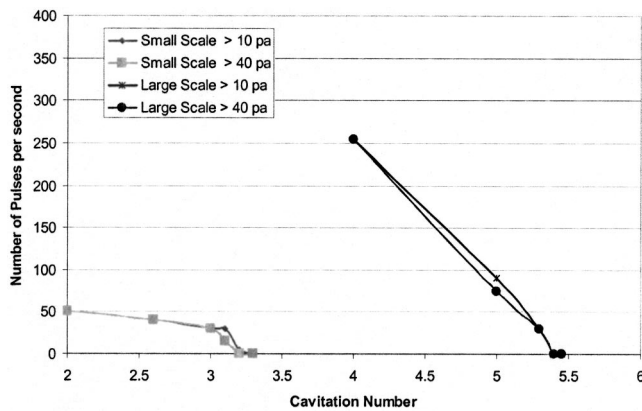


Fig. 17 Number of pressure peaks versus cavitation number deduced at two criteria of acoustic level for the small and large scales considered

Table 3 Cavitation inception numbers obtained from the numerical study using various criteria, and power law fit deduced from these results. For smaller void fraction ( $\alpha \approx 1 \times 10^{-9}$ ).

	Numerical computed values for $\sigma_i$		$R_c^\gamma$ curve fit $\gamma$
	Small Scale	Large Scale	
$-Cp_{\min}$	3.34	5.48	0.357
10 peaks/s over 10 Pa	3.20	5.40	0.377
50 peaks/s over 40 Pa	2.0	5.18	0.687

nuclei size range. Two acoustic pressure levels, 10 and 40 Pa, are also selected to determine the number of pressure peaks for each cavitation number. The resulting curves of number of pressure peaks versus cavitation numbers for the small and large scales are shown in Fig. 17. The deduced cavitation inception numbers are shown in Table 3. By comparing with Table 2 we can see very important differences for the small scale when the cavitation inception criteria are less stringent. Also, scaling effects and deviation from classical formula due to nuclei size distribution are seen to significantly increase when nuclei sizes (or void fraction) decreases.

## 4 Conclusions

The study of the behavior of a realistic distribution of nuclei in the tip vortex flow field of a NACA16020 foil at three scales has enabled observation of several effects:

1. Comparison of the size of the bubble capture area or “window of opportunity” at the various scales shows that the larger scale results in more cavitation events by allowing more nuclei per unit time to be captured by the tip vortex;
2. the numerical results show that different criteria for defining the cavitation inception can lead to a different cavitation inception numbers as well as different scaling laws. By comparing the predicted cavitation inception number with  $-Cp_{\min}$ , we found that scaling effects (i.e., deviation from  $-Cp_{\min}$ ) due to nuclei increase as the reference inception criteria become less stringent (higher reference pressure amplitude and larger number of peaks);
3. the predicted value of  $\gamma$  in the power formula ( $\sigma_i \propto R_c^\gamma$ ) is closer to the classical value ( $\gamma=0.4$ ), as the reference inception criterion becomes less stringent;
4. the range of nuclei sizes was shown to have an important effect on the prediction of cavitation inception. Differences between predicted cavitation inception number and  $-Cp_{\min}$  increase as nuclei sizes (or void fractions) decrease. This implies that scaling effects due to nuclei size distribution are stronger when the water contains only small nuclei (or for low void fraction).

## Acknowledgments

This work was conducted at Dynaflo, Inc. ([www.dynaflo-inc.com](http://www.dynaflo-inc.com)) and has been supported by the Naval Surface Warfare Carderock Division and the Office of Naval Research. This support of Dr. Ki-Han Kim, ONR, and Dr. Young Shen, NSWCCD, is greatly appreciated.

## References

- [1] McCormick, B. W., 1962, “On Cavitation Produced by a Vortex Trailing From a Lifting Surface,” *ASME J. Basic Eng.*, **84**, pp. 369–379.
- [2] Fruman, D. H., Dugue, C., Pauchel, A., and Cerrutti, P., 1992, “Tip Vortex Roll-Up and Cavitation,” *Eighteenth Symposium on Naval Hydrodynamics*, Seoul, Korea.
- [3] Arndt, R. E., and Dugue, C., 1992, “Recent Advances in Tip Vortex Cavitation Research,” *Proc. International Symposium on Propulsors Cavitation*, Hamburg, Germany, pp. 142–149.
- [4] Farrell, K. J., and Billet, M. L., 1994, “A Correlation of Leakage Vortex Cavitation in Axial-Flow Pumps,” *ASME J. Fluids Eng.*, **116**, pp. 551–557.
- [5] Maines, B., and Arndt, R., 1997, “Tip Vortex Formation and Cavitation,” *ASME J. Fluids Eng.*, **119**, pp. 413–419.
- [6] Arndt, R. E. A., 2002, “Cavitation in Vertical Flows,” *Annu. Rev. Fluid Mech.*, **34**, pp. 143–175.
- [7] Copalan, S., Liu, H. L., and Katz, J., 2000, “On the Flow Structure, Tip Leakage Cavitation Inception and Associated Noise,” 23rd Symposium on Naval Hydrodynamics.
- [8] Hsiao, C.-T., Chahine, G. L., and Liu, H. L., 2003, “Scaling Effects on Prediction of Cavitation Inception in a Line Vortex Flow,” *ASME J. Fluids Eng.*, **125**, pp. 53–60.
- [9] Ligneul, P., and Latorre, R., 1989, “Study on the Capture and Noise of Spherical Nuclei in the Presence of the Tip Vortex of Hydrofoils and Propellers,” *Acustica*, **68**, pp. 1–14.
- [10] Hsiao, C.-T., and Pauley, L. L., 1999, “Study of Tip Vortex Cavitation Inception Using Navier–Stokes Computation and Bubble Dynamics Model,” *ASME J. Fluids Eng.*, **121**, pp. 198–204.
- [11] Hsiao, C.-T., and Chahine, G. L., 2004, “Prediction of Vortex Cavitation Inception Using Coupled Spherical and Nonspherical Models and UnRANS Computations,” *J. Marine Sci. Technol.*, **8**, No. 3, pp. 99–108.
- [12] Arndt, R. E. A., and Maines, B. H., 2000, “Nucleation and Bubble Dynamics in Vortical Flows,” *ASME J. Fluids Eng.*, **122**, pp. 488–493.
- [13] Hsiao, C.-T., and Pauley, L. L., 1999, “Study of Tip Vortex Cavitation Inception Using Navier–Stokes Computation and Bubble Dynamics Model,” *ASME J. Fluids Eng.*, **121**, pp. 198–204.
- [14] Hsiao, C.-T., and Pauley, L. L., 1998, “Numerical Study of the Steady-State Tip Vortex Flow Over a Finite-Span Hydrofoil,” *ASME J. Fluids Eng.*, **120**, pp. 345–349.
- [15] Hsiao, C.-T., and Pauley, L. L., 1999, “Numerical Calculation of Tip Vortex Flow Generated by a Marine Propeller,” *ASME J. Fluids Eng.*, **121**, pp. 638–645.
- [16] Taylor, L. K., Pankajakshan, R., Jiang, M., Sheng, C., Briley, W. R., Whitfield, D. L., Davoudzadeh, F., Boger, D. A., Gibeling, H. J., Gorski, J., Haussling,

- H., Coleman, R., and Buley, G., 1998, "Large-Scale Simulations for Maneuvering Submarines and Propulsors," AIAA Paper 98-2930.
- [17] Chorin, A. J., 1967, "A Numerical Method for Solving Incompressible Viscous Flow Problems," *J. Comput. Phys.*, **2**, pp. 12–26.
- [18] Roe, P. L., 1981, "Approximate Riemann Solvers, Parameter Vectors, and Difference Schemes," *J. Comput. Phys.*, **43**, pp. 357–372.
- [19] van Leer, B., 1979, "Towards the Ultimate Conservative Difference Scheme V. A Second Order Sequel to Godunov's Method," *J. Comput. Phys.*, **32**, pp. 101–136.
- [20] Vanden, K., and Whitfield, D. L., 1993, "Direct and Iterative Algorithms for the Three-Dimensional Euler Equations," AIAA-93-3378.
- [21] Chahine, G. L., Kalumuck, K. M., Cheng, L.-Y., and Frederick, G., 2001, "Validation of Bubble Distribution Measurements of the ABS Acoustic Bubble Spectrometer With High Speed Video Photography," *4th International Symposium on Cavitation*, California Institute of Technology, Pasadena, CA.
- [22] Johnson, V. E., and Hsieh, T., 1966, "The Influence of the Trajectories of Gas Nuclei on Cavitation Inception," *Sixth Symposium on Naval Hydrodynamics*, pp. 163–179.
- [23] Haberman, W. L., and Morton, R. K., 1953, "An Experimental Investigation of the Drag and Shape of Air Bubbles Rising in Various Liquids," Report 802, DTMB.
- [24] Fitzpatrick, N., and Strasberg, M., 1958, "Hydrodynamic Sources of Sound," *2nd Symposium on Naval Hydrodynamics*, pp. 201–205.
- [25] Dacles-Mariani, J., Zilliac, G. G., Chow, J. S., and Bradshaw, P., 1995, "Numerical/Experimental Study of a Wingtip Vortex in the Near Field," *AIAA J.*, **33**, No. 9, pp. 1561–1568.
- [26] Billet, M. L., 1984, "Cavitation Nuclei Measurements," *International Symposium on Cavitation Inception*, FED-Vol. 16, pp. 33–42.
- [27] Franklin, R. E., 1992, "A Note on the Radius Distribution Function for Microbubbles of Gas in Water," *ASME Cavitation and Multiphase Flow Forum*, FED-Vol. 135, pp. 77–85.